Magnetic Resonance Imaging 80 (2021) 132–143

Contents lists available at ScienceDirect

Magnetic Resonance Imaging

journal homepage: www.elsevier.com/locate/mri

Rapid microscopic fractional anisotropy imaging via an optimized linear regression formulation

N.J.J. Arezza [a,b,*], D.H.Y. Tse [a], C.A. Baron [a,b]

[a] Centre for Functional and Metabolic Mapping (CFMM), Robarts Research Institute, University of Western Ontario, London, Canada
[b] Department of Medical Biophysics, Schulich School of Medicine and Dentistry, University of Western Ontario, London, Canada

ARTICLE INFO

Keywords:
Diffusion weighted imaging
Microscopic anisotropy
Microscopic fractional anisotropy
Microstructure
Neuroimaging

ABSTRACT

Water diffusion anisotropy in the human brain is affected by disease, trauma, and development. Microscopic fractional anisotropy (μFA) is a diffusion MRI (dMRI) metric that can quantify water diffusion anisotropy independent of neuron fiber orientation dispersion. However, there are several different techniques to estimate μFA and few have demonstrated full brain imaging capabilities within clinically viable scan times and resolutions. Here, we present an optimized spherical tensor encoding (STE) technique to acquire μFA directly from the 2nd order cumulant expansion of the powder averaged dMRI signal obtained from direct linear regression (i.e. diffusion kurtosis) which requires fewer powder-averaged signals than other STE fitting techniques and can be rapidly computed. We found that the optimal dMRI parameters for white matter μFA imaging were a maximum b-value of 2000 s/mm^2 and a ratio of STE to LTE tensor encoded acquisitions of 1.7 for our system specifications. We then compared two implementations of the direct regression approach to the well-established gamma model in 4 healthy volunteers on a 3 Tesla system. One implementation used mean diffusivity (D) obtained from a 2nd order fit of the cumulant expansion, while the other used a linear estimation of D from the low b-values. Both implementations of the direct regression approach showed strong linear correlations with the gamma model ($\rho = 0.97$ and $\rho = 0.90$) but mean biases of -0.11 and -0.02 relative to the gamma model were also observed, respectively. All three μFA measurements showed good test-retest reliability ($\rho \geq 0.79$ and bias $= 0$). To demonstrate the potential scan time advantage of the direct approach, 2 mm isotropic resolution μFA was demonstrated over a 10 cm slab using a subsampled data set with fewer powder-averaged signals that would correspond to a 3.3-min scan. Accordingly, our results introduce an optimization procedure that has enabled nearly full brain μFA in only several minutes.

1. Introduction

Diffusion MRI (dMRI) can noninvasively acquire information about the microstructural characteristics of biological systems by probing the displacement of water molecules in tissue [1,2]. Microstructural features that affect the apparent diffusion rate of water include cell size, shape, density, orientation, and the presence of membranes and barriers; thus, dMRI has found use in the study of neurological diseases that alter tissue microstructure [3–6].

The most commonly used dMRI technique is diffusion tensor imaging (DTI) [7], in which dMRI data is fitted to the diffusion tensor model to estimate metrics such as the mean diffusivity (D) and fractional anisotropy (FA). DTI represents the dMRI signal as being entirely characterized by Gaussian diffusion [8], implicitly meaning the logarithm of the dMRI signal is assumed to depend on the b-value up to the first order in the cumulant expansion [9]. However, diffusion in tissues is too complex to be fully represented by Gaussian diffusion at high b-values [10], and characterizing the"non-Gaussian" signal provides more information about the underlying tissue [11–13]. Diffusion kurtosis imaging (DKI) was developed to capture the effects of non-Gaussian diffusion by expanding the dMRI signal using cumulants up to second order in b-value [14]. Generally, DKI has been shown to be more sensitive than DTI towards quantifying microstructural changes that result from disease [15–17].

Non-Gaussian diffusion can be attributed to a number of sources including isotropic kurtosis from polydisperse diffusion tensors with different mean diffusivities, anisotropic kurtosis from diffusion tensors dispersed among multiple orientations, time-dependent diffusion [18],

* Corresponding author at: Robarts Research Institute, Western University, 1151 Richmond St. N., London, ON N6A 5B7, Canada.
E-mail address: narezza@uwo.ca (N.J.J. Arezza).

https://doi.org/10.1016/j.mri.2021.04.015
Received 24 February 2021; Received in revised form 1 April 2021; Accepted 29 April 2021
Available online 1 May 2021

and microscopic kurtosis from restricted diffusion and microscopic structural disorder [12,18–20]. Unfortunately, both DTI and DKI are unable to distinguish between true microstructural changes and neuron fiber orientation dispersion, reducing their specificity to disease in brain regions containing crossing or fanning axons [21,22]. While DTI does not consider the effects of kurtosis at all, DKI cannot differentiate between any of the different sources of kurtosis without imposing assumptions about the underlying tissue [14,23].

In recent years, efforts have been made to develop dMRI techniques that can quantify water diffusion anisotropy independent of orientation dispersion [24,25]. Microscopic anisotropy (μA) is an anisotropy metric that is independent of both reference frame and orientation dispersion, and microscopic fractional anisotropy (μFA) is a normalized variation of μA that additionally aims to remove the dependence on compartment size [26]. There are multiple techniques to compute μFA, which can be categorized into: (1) methods that involve the use of linear tensor encoding (LTE) sequences [27–29], (2) methods that utilize double diffusion encoding (DDE) [30], and (3) methods that use nonconventional continuous gradient waveforms such as spherical tensor encoding (STE) [22,25,31–33].

LTE methods utilize models to decouple microstructural properties from mesoscopic tissue orientation [34]. These techniques require prior knowledge or estimates of tissue properties such as the axonal volume fraction or the intracellular radial diffusivity [34] but are highly accessible because LTE sequences are commonly used in both DTI and DKI. Generally, anisotropy can be estimated by acquiring LTE signals across multiple directions and b-shells and fitting the powder-averaged signals to a constrained model such as the spherical mean technique (SMT) model [28,29]. Recently, Henriques et al. showed that μFA estimations using LTE are inaccurate compared to ground truth anisotropy, suggesting the techniques are not robust or do not sufficiently describe the underlying microstructure [34].

DDE techniques to estimate μA and μFA use two independent diffusion-encoding pulse vectors in succession to probe the correlation of water diffusion in different directions [24,35–38]. DDE can distinguish between microstructural properties and orientation dispersion without imposing modeling constraints [30,35], likely making the technique more robust and accurate than LTE techniques by eliminating the possibility of assumption misestimation. Furthermore, the clinical viability of DDE μFA imaging was demonstrated in a preliminary study of multiple sclerosis (MS) patients at 3 T with a 5 min scan time and 3 mm isotropic resolution [39], and the minimalistic sampling scheme used in that work was further validated [40]. While DDE is a promising technique, it has some limitations. Due to the use of two consecutive diffusion-encoding pulses separated by a mixing time, DDE sequences require longer TEs than standard LTE sequences to achieve equal b-values. Furthermore, a twice-refocused implementation is required to avoid biases due to concomitant fields [41,42], further increasing the TE. A notable example of a DDE technique to estimate μFA is correlation tensor imaging (CTI) [19].

Techniques that utilize nonconventional diffusion-encoding waveforms probe unique q-space trajectories that provide additional information about tissue microstructure beyond the capabilities of LTE. In STE-based methods, signal variance due to non-Gaussian diffusion is characterized into two sources: isotropic variance arising from polydispersity in mean diffusivity, and anisotropic variance arising from microscopic anisotropy [22]; a general assumption underlying these techniques is that LTE signal depends on both isotropic and anisotropic variance while STE signals depend only on isotropic variance (i.e., time dependent diffusion and microscopic kurtosis are ignored). STE-based μFA protocols use unique waveforms to acquire single-shot STE diffusion weighted signals [25,43]. Though more TE-efficient than DDE, STE waveforms can potentially introduce time-dependent effects due to varying spectral content over the different gradient channels [43]. Furthermore, STE-based techniques assume that the dMRI signal contains only Gaussian compartments, which is an approximation that more advanced techniques like CTI avoid [19]. Some examples of techniques that use STE acquisitions to estimate μFA and other parameters are the gamma model, in which the inverse Laplace transform of the gamma distribution is fitted to powder averaged dMRI signals from LTE acquisitions and STE acquisitions [22,44], and direct linear regression of the cumulant expansion of the diffusion signal [32,45,46].

The application of μFA imaging to clinical research is appealing due to the unique insight it may provide into brain microstructure; for example, preliminary studies have found that μFA can better distinguish between different types of brain tumors than FA and other MRI metrics [22] and that it provides improved delineation of MS lesions over FA as well as unique contrast compared to T1- and T2-weighted imaging [39]. The parameter's insensitivity to orientation dispersion is advantageous over FA in the study or diagnosis of neuropathology in brain regions containing crossing or fanning fibers. However, μFA generally requires long scan times that are not clinically feasible, especially when used in conjunction with other imaging techniques that are required in the clinical workflow. Other demonstrations of μFA that have achieved shorter scan times did so at the cost of resolution [39,47], producing μFA maps with poorer resolution than typical FA maps acquired with DTI. To maximize scan efficiency, it is essential to understand the optimal parameters required to measure μFA and use this information to design rapid protocols. To our knowledge, no comprehensive assessment of the optimal choices of b-value and relative numbers of LTE and STE acquisitions have been performed.

The aims of this work were to optimize a protocol for acquiring μFA within a clinically viable scan time of <5 mins using the linear regression approach, and to demonstrate the feasibility of this method by comparing it to the highly cited gamma model. We investigated the optimal b-values and ratio of STE to LTE acquisitions for the estimation of μFA in white matter and combined these findings with two implementations of direct linear regression to enable the acquisition of full-brain, 2 mm isotropic resolution μA and μFA maps in vivo within a 3.3 min scan time and a 2-min computation time. Estimates of μFA using direct approaches strongly correlated with the gamma model in white matter regions ($\rho \geq 0.9$), and all approaches exhibited high test-retest reliability ($\rho \geq 0.77$).

2. Theory

2.1. μFA estimation

The normalized signal intensity of powder-averaged dMRI acquisitions of a multi-component system, assuming negligible time-dependent diffusion, can be represented by the cumulant expansion [25]:

$$ln\left(\frac{S}{S_0}\right) = -Db + \frac{\mu_2}{2}b^2 \ldots \quad (1)$$

where S is the powder-averaged signal, S_0 is the mean signal with no diffusion encoding, b is the b-value, and μ_2 is the second central moment or variance of diffusivity. Lasic et al. [25] define the microscopic fractional anisotropy in terms of the scaled difference in variance between powder-average LTE and STE acquisitions:

$$\mu FA = \sqrt{\frac{3}{2}}\left(1 + \frac{2}{5}\frac{1}{\Delta\widetilde{\mu_2}}\right)^{-\frac{1}{2}} \quad (2)$$

$$\Delta\widetilde{\mu_2} = \frac{\mu_2^{LTE} - \mu_2^{STE}}{D^2} \quad (3)$$

where μ_2^{LTE} and μ_2^{STE} are the second terms in the cumulant expansions of powder-averaged LTE and STE acquisitions, respectively. Using eq. (1) up to the second cumulant term, the powder-averaged LTE and mean STE signals can be represented as:

$$S_{LTE} = S_0 e^{-Db+\frac{\mu_2^{LTE}}{2}b^2} \tag{4}$$

$$S_{STE} = S_0 e^{-Db+\frac{\mu_2^{STE}}{2}b^2} \tag{5}$$

If it is assumed that the only sources of kurtosis are dispersion in size and orientation of diffusion tensors, then the diffusion coefficient D will be equal between LTE and STE [22]. By assuming D is the same between LTE and STE signals acquired at the same b-value, eqs. (4, 5) can be substituted into eq. (3) to provide an estimate of the scaled difference in variance that notably does not depend on the non-diffusion weighted signal S_0:

$$\Delta\widetilde{\mu_2} = \frac{2ln(S_{LTE}/S_{STE})}{D^2b^2} \tag{6}$$

Substituting eq. (6) into eq. (1) provides an estimate of the μFA [46]:

$$\mu FA = \sqrt{\frac{3}{2}}\left(1+\frac{D^2b^2}{5ln\left(\frac{S_{LTE}}{S_{STE}}\right)}\right)^{-\frac{1}{2}} \tag{7}$$

Microscopic anisotropy is defined here based on the difference in signal between LTE and STE dMRI acquisitions, similar to the equation used in DDE protocols [36]:

$$\mu A = \sqrt{\frac{ln\left(\frac{S_{LTE}}{S_{STE}}\right)}{b^2}} \tag{8}$$

By ignoring the third and higher order cumulant terms in deriving eqs. (4, 5), μA can be estimated from a single b-shell, reducing scan time; however, ignoring the higher cumulants comes with the cost of potentially introducing a bias to the measurement [48]. μFA can then be expressed in terms of μA by substituting eq. (8) into eq. (7):

$$\mu FA = \sqrt{\frac{3}{2}\frac{\mu A^2}{\mu A^2 + 0.2D^2}} \tag{9}$$

2.2. Diffusion coefficient estimation using the diffusion kurtosis model

Explicitly enforcing that the diffusion coefficient D is the same between LTE and STE acquisitions causes the minimum number of powder-averaged samples required to estimate the four unknowns in eqs. (4, 5), S_0, D, μ_2^{LTE} and μ_2^{STE}, in a joint least squares estimation to be only four (with at least one non-zero b-value sampled for each of LTE and STE). For example, a protocol could contain LTE and STE acquisitions at a single high b-value (e.g., 2000 s/mm^2), plus either STE or LTE acquisitions at two smaller b-values (e.g., STE at b = 0 and STE at b = 1000 s/mm^2). Contrary to previously proposed approaches, both STE and LTE would *not* be required in each shell using this joint estimation approach. Then, μA^2 could be estimated from μ_2^{LTE} and μ_2^{STE} using eq. (3), and μFA estimated from eq. 9. This approach will be referred to as "joint linear regression". Alternatively, μA^2 could be estimated directly from the STE and LTE acquisitions at the highest b-value (e.g., 2000 s/mm^2) using eq. (8) while D could be estimated using a linear fit over the low b-values (e.g., LTE at b = 0 and LTE at b = 1000 s/mm^2). Ignoring kurtosis in the estimation of D may introduce a bias, but this approach is extremely computationally efficient which may improve clinical relevance. This will be referred to as "simplified regression".

2.3. μA optimization

To optimize a protocol for μA and μFA, sequence parameters that maximize the ratio of the mean measurement to its standard deviation can be evaluated, similar to the approach used to determine optimal parameters for diffusivity measurements [49]. Using standard error propagation [50], the signal-to-noise ratio (SNR) of a μFA image generated using eq. (9) can be related to the variance in μA^2 and D, with μFA image quality increasing with reduced variance in μA^2 and D measurements. It is expected that μA^2 will generally have much higher variance than D because it depends only on the highest b-shell data (eq. (8)), which has the lowest SNR. Thus, we will focus on the optimization of μA^2 as a surrogate for the optimization of μFA. The SNR of a μA^2 image can be expressed as (Appendix):

$$\frac{\mu A^2}{\sigma_{\mu A^2}} = \frac{ln\left(\frac{S_{LTE}}{S_{STE}}\right)\sqrt{n_{LTE}n_{STE}}S_{LTE}S_{STE}}{\sigma\sqrt{n_{LTE}S_{LTE}^2 + n_{STE}S_{STE}^2}} \tag{10}$$

where n_{LTE} is the number of LTE directions acquired, n_{STE} is the number of STE averages acquired, S_{LTE} and S_{STE} are the powder-averaged signals of the LTE and STE images, respectively, and σ is the mean image noise. Given that $\mu A^2/\sigma_{\mu A2}$ is maximized when $n_{STE}/n_{LTE} = S_{LTE}/S_{STE}$ (see Appendix), and that S_{LTE} and S_{STE} are dependent on b-value, the optimal protocol parameters (b and n_{STE}/n_{LTE}) can be determined using eq. (10).

Eqs. (4, 5) can be substituted into eq. (10), and assuming all STE and LTE acquisitions are performed with the same TE:

$$\frac{\mu A^2}{\sigma_{\mu A^2}} = e^{-\frac{TE(b)}{T2}}\frac{b^2\sqrt{n_{LTE}n_{STE}}\left(\frac{\mu_2^{LTE}-\mu_2^{STE}}{2}\right)\left(e^{-Db+b^2\left(\frac{\mu_2^{LTE}+\mu_2^{STE}}{2}\right)}\right)}{\sigma\sqrt{\left((n_{LTE})e^{b^2\left(\mu_2^{LTE}\right)}+(n_{STE})e^{b^2\left(\mu_2^{STE}\right)}\right)}} \tag{11}$$

Eq. (11) reveals that the SNR depends on TE(b) by an exponential prefactor. Note that the TE is a function of the b-value, as higher b-value acquisitions will require longer TEs.

3. Methods

Two sets of MRI scans were performed on two sets of volunteers for this work. The study was approved by the Institutional Review Board at Western University and informed consent was obtained from each volunteer prior to scanning. The first set of scans (3.1) consisted of LTE and STE acquisitions over a wide range of b-values and was acquired to provide the signal data needed to optimize μA using eq. (10). The second set of scans (3.2, 3.3) performed test-retest measurements with a comprehensive sequence that allowed for μFA mapping using the gamma model, joint linear regression (section 2.2), and simplified linear regression (section 2.2). The various dMRI sequences and data subsets are summarized in Table 1 and are described in detail below.

3.1. Sequence optimization

MRI scans were performed in 4 healthy volunteers (2 female and 2 male, mean age 22.4 ± 1.7 years) on a 3 T Prisma whole-body MR system (Siemens Healthineers) with 80 mT/m strength and 200 T/m/s slew rate. Multiple b-shell diffusion data were acquired in a single scan using LTE and STE sequences: 6 image volumes were acquired at b = 0 s/mm^2, and 6 LTE directions and 6 STE averages were acquired at b-values between 500 and 3500 s/mm^2, in increments of 500 s/mm^2. The STE sequence was designed to avoid net phase accumulation from concomitant fields by using trapezoidal gradient schemes that are symmetric about a 180° pulse (Fig. 1) [41], while a standard pulsed gradient spin echo sequence was used for LTE acquisitions [1]. The other parameters were TE/TR = 125/8700 ms, FOV = 192 × 192 mm^2, 2 mm isotropic resolution, 45 slices, rate 2 GRAPPA, 2 averages, and total scan time = 29 min. Images were processed using Gibbs ringing correction and Eddy current correction with FSL Eddy [51].

A region of interest (ROI) across multiple slices was manually selected in the frontal WM for each patient and used to measure the mean LTE signal and mean STE signal at each b-value. A joint regression

Table 1
Summary of MRI sequences and data subsets for in vivo acquisitions.

	Sequence optimization	Comprehensive
TE/TR (ms)	125/8700	94/4500
Slices	45 axial	48 axial
Parallel Imaging	$R = 2$ in-plane	R = 2 in-plane, 2 SMS (4 total)
Resolution (mm^3)	2 × 2 × 2	2 × 2 × 2
Diffusion scheme	0 s/mm^2 (6 LTE)	0 s/mm^2 (5 LTE)
	500 s/mm^2 (6 LTE + 6 STE)	100 s/mm^2 (3 LTE + 6 STE)
	1000 s/mm^2 (6 LTE + 6 STE)	700 s/mm^2 (3 LTE + 6 STE)
	1500 s/mm^2 (6 LTE + 6 STE)	1000 s/mm^2 (15 LTE + 10 STE)
	2000 s/mm^2 (6 LTE + 6 STE)	1400 s/mm^2 (6 LTE + 10 STE)
	2500 s/mm^2 (6 LTE + 6 STE)	2000 s/mm^2 (22 LTE + 27 STE)
	3000 s/mm^2 (6 LTE + 6 STE)	
	3500 s/mm^2 (6 LTE + 6 STE)	
	Data subsets	
Optimization validation (no denoising)	–	***Suboptimal subset***
		100 s/mm^2 (3 LTE + 6 STE)
		700 s/mm^2 (3 LTE + 6 STE)
		1400 s/mm^2 (6 LTE + 10 STE)
		2000 s/mm^2 (16 LTE + 6 STE)
		Standard subset
		100 s/mm^2 (3 LTE + 6 STE)
		700 s/mm^2 (3 LTE + 6 STE)
		1400 s/mm^2 (6 LTE + 10 STE)
		2000 s/mm^2 (6 LTE + 16 STE)
Model comparisons (denoised)	–	***Standard subset***
		**Same as standard subset above*
		Simplified subset
		100 s/mm^2 (3 LTE)
		1000 s/mm^2 (15 LTE)
		2000 s/mm^2 (16 LTE + 22 STE)
Minimalistic sequence (denoised)	–	100 s/mm^2 (3 STE)
		1000 s/mm^2 (6 STE)
		2000 s/mm^2 (16 LTE + 18 STE)

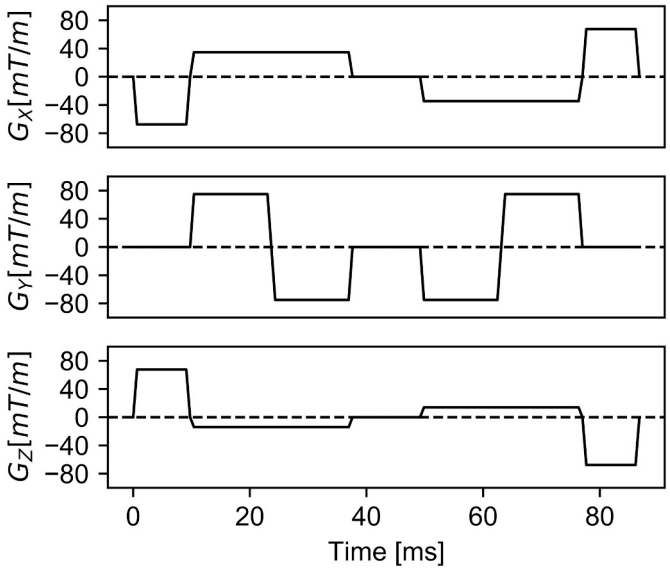

Fig. 1. Schematic representation of the spherical tensor encoding gradient waveforms. Diffusion encoding blocks have been inserted on both sides of a 180° pulse in all three gradient directions to acquire an STE diffusion MRI signal. Implicit gradient reversal due to the 180° pulse has been applied.

was performed on the mean LTE and STE signal data to fit the curves to eq. (1) up to the third cumulant, with the assumption that D is the same in LTE and STE acquisitions. The best-fit cumulant expansions for each of the 4 volunteers were averaged and used together with eq. (10) to determine the optimal b-value and optimal ratio of LTE to STE acquisitions in a μA protocol. In evaluation of eq. (10), the T2 decay constant was assumed to be 80 ms to approximate WM at 3 T [52]. These SNR calculations assume the same total number of acquisitions at each b-value, with only the ratio of n_{STE}/n_{LTE} acquisitions changing.

3.2. Comprehensive acquisitions

A comprehensive 113 acquisition dMRI protocol was used to acquire the data to compare μFA volumes generated with different methods. 4 healthy volunteers (2 female and 2 male, mean age 28.0 ± 6.6 years) were imaged at 3 T with a 9-min dMRI scan with TE/TR = 94/4500 ms. The scan consisted of 3, 3, 15, 6, and 22 LTE directions and 6, 6, 10, 10, and 27 STE averages at b = 100, 700, 1000, 1400, and 2000 s/mm^2, respectively, as well as 5 averages at b = 0 s/mm^2. These directions were chosen to enable retrospective splitting of the data into the subsets described below. The other parameters were FOV = 220 × 220 mm^2, 2 mm isotropic resolution, 48 slices, and rate 2 in-plane parallel imaging combined with rate 2 simultaneous multislice (SMS). Volunteers were also scanned using T1-weighted MPRAGE with 1 mm isotropic resolution. After removing each volunteer from the MR scanner for a period of 5–10 min, a repeat measurement was performed using only the dMRI protocol. Data from these acquisitions is available online [dataset] [53].

Two separate post-processing pipelines were performed on the data to acquire two different data sets: a “noisy” data set that omitted denoising to test the effects of using an optimized vs. suboptimal ratio of STE to LTE scans to compute μA, since denoising is a non-linear operation that invalidates the assumptions used in the derivation of eq. (10), and a denoised data set to compare the μFA approaches described in section 2.2 to the gamma model. All the diffusion MRI data was processed using Gibbs ringing correction and FSL Eddy [51], and PCA denoising [54] was performed prior to these corrections for the denoised data set.

The T1-weighted anatomical volumes were segmented into WM and grey matter (GM) masks using FMRIB’s Automated Segmentation Tool (FAST) [55] and were registered to the denoised dMRI volumes using

symmetric diffeomorphic and affine transforms with ANTS software (https://github.com/ANTsX/ANTs) [56]. The retest noisy and denoised volumes were also registered to the respective test volumes using a rigid transform with ANTS.

To validate eq. (10), the noisy dMRI data was split into two 56-acquisition subsets to represent a standard protocol that approximately complies with our optimization results and a suboptimal protocol that does not comply. The standard protocol was based on a rapid sequence proposed by Nilsson et al. [47] and included 3, 3, 6, and 6 LTE directions and 6, 6, 10, and 16 STE averages at b = 100, 700, 1400, and 2000 s/mm^2. The suboptimal protocol consisted of the same acquisitions with one exception: the ratio n_{iso}/n_{lin} at the b = 2000 s/mm^2 shell was 6/16 instead of 16/6, a suboptimal ratio (see 4.1). The 6 direction subset of LTE acquisitions used an icosahedral sampling scheme [47], and the 16 direction subset was distributed using electrostatic repulsion [57]. Notably, no denoising was applied to these data subsets.

To compare linear regression to the gamma model, the denoised dMRI data was split into two subsets with each containing 56 acquisitions. The standard subset, to be used to compare the gamma model versus joint linear regression (section 2.2), used the rapid sequence by Nilsson et al. described above [47]. An additional subset, referred to herein as the "simplified subset", included 22 STE averages at b = 2000 s/mm^2 and 3, 15, and 16 LTE directions at b = 100, 1000, and 2000 s/mm^2 (56 total acquisitions), and was designed to investigate whether a single b-shell to compute μA^2 (b = 2000 s/mm^2) can be added to a DTI acquisition (b = 100, 1000 s/mm^2) to enable μFA imaging using the simplified regression approach described in section 2.2. The b = 1000 and 2000 s/mm^2 LTE shells were determined separately from each other using electrostatic repulsion.

An additional subset of the comprehensive scan containing 43 acquisitions was used to demonstrate the potential scan time advantage of the linear regression technique. This "minimalistic subset" contained 16 LTE directions at b = 2000 s/mm^2 and 3, 6, and 18 STE averages at b = 100, 1000, and 2000 s/mm^2, respectively, and would have required only 3.3 min of scan time.

3.3. Analysis

To validate eq. (1), the SNR of μA^2 was compared between the standard and suboptimal subsets of the noisy dMRI data by first estimating μA^2 at b = 2000 s/mm^2 in both the test and retest volumes for each volunteer. Then, the test-retest coefficients of variance (CoVs) of the standard and suboptimal volumes across all volunteers were compared as a surrogate of SNR.

For model comparisons with the denoised data, the powder-averaged STE and LTE signals vs. b-value were fitted to the diffusion kurtosis model using a joint non-negative least squares method assuming consistent D between STE and LTE, and μFA was computed using eq. (2) (μFA$_{joint}$). μFA was also estimated using Nilsson et al.'s Multidimensional diffusion MRI software [58] (https://github.com/markus-nilsson/md-dmri) to fit the diffusion-weighted signals to the gamma model (μFA$_{gamma}$). μFA maps were generated for each volunteer using these two methods in the standard subset of data.

Additionally, μFA was estimated using eq. (9) in the simplified subset by decoupling μA^2 and D (μFA$_{simp}$): μA^2 was estimated at b = 2000 s/mm^2 using the direct cumulant method (eq. (8)) while D was estimated by fitting the b = 100 and 1000 s/mm^2 LTE data to the DTI model using FMRIB's DTIFIT tool.

The μFA maps from the different methods and subsets were then compared in WM using Bland-Altman plots and voxelwise scatter plots, and Pearson correlation coefficients were computed between each technique. To test the repeatability of the measurement techniques, Bland-Altman plots were generated for each patient to compare the initial and repeat μFA volumes and Pearson correlation coefficients were computed between initial and repeat μFA maps.

The minimalistic subsets were used to generate full-brain μFA maps using the joint regression approach (section 2.2), and the repeatability of this measurement technique was assessed using the methods described above. The maps generated using these subsets were not compared to the gamma model as they contained too few b-shells for gamma model fitting.

4. Results

4.1. Sequence optimization

The logarithm of the powder-averaged WM dMRI signal as a function of b-value, averaged across all volunteers, is shown in Fig. 2. As expected [22], the departure from monoexponential signal decay was greater in the LTE than STE signal curve due to the mesoscopic orientation of tensors. Fig. 3 shows the variation in $\mu A^2/\sigma_{\mu A2}$ with b-value and the ratio of n_{STE}/n_{LTE} assuming a fixed total number of acquisitions ($n_{STE} + n_{LTE}$). For any given b-value, the optimal n_{STE}/n_{LTE} was computed to be equal to the ratio of the powder averaged signals, S_{LTE}/S_{STE}, at said b-shell. The highest $\mu A^2/\sigma_{\mu A2}$ occurred when the b-value was 2000 s/mm^2, for which the optimal n_{STE}/n_{LTE} was approximately 1.7. However, a wide range of dMRI parameter configurations yielded an SNR above 95% of the optimal parameters for μA^2 SNR.

A significant drop off in SNR occurred for $n_{STE}/n_{LTE} < 1$, suggesting that image quality is maximized when the number of STE acquisitions is greater than or equal to the number of LTE acquisitions. The suboptimal dataset is located in this region where the SNR sharply decreases, while the standard data set is in the high SNR region that varies slowly. Using the powder averaged STE and LTE WM signal data from the noisy data subset at b = 2000 s/mm^2 across all volunteers along with eq. (10), the SNR of μA^2 in the suboptimal subset was predicted to be 87% of the SNR of μA^2 in the standard subset. Analysis of the test and retest μA^2 volumes revealed a CoV of 22.94% in the standard measurement and a CoV of 25.78% in the suboptimal measurement, yielding an experimentally acquired SNR ratio of approximately 89% (since CoV is analogous to SNR^{-1}) which is comparable to the value of 87% predicted by eq. (10). Example μA^2 images estimated using the standard and suboptimal subsets are depicted in Fig. 4.

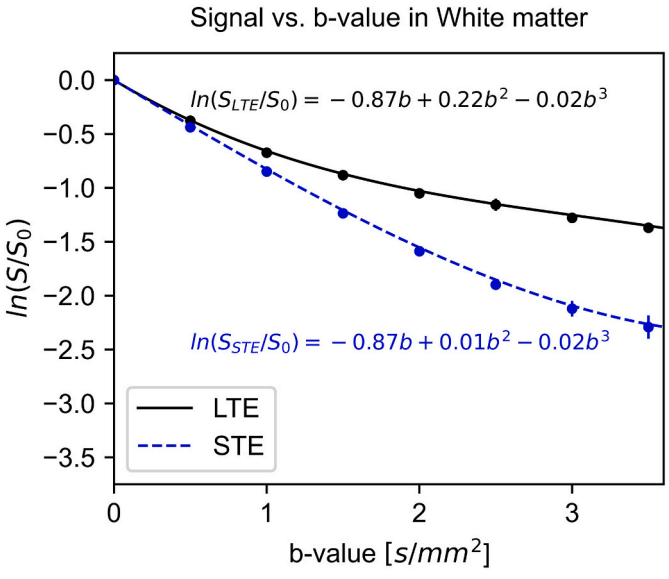

Fig. 2. Logarithm of the diffusion MRI signal vs. b-value in frontal white matter. The plot shows the powder-averaged signal from a manually prescribed region of interest across four volunteers as measured with linear tensor encoding and spherical tensor encoding (black and blue circles, respectively), while the lines show the third order cumulant model fit. Also depicted are the standard deviations across the volunteers. (For interpretation of the references to colour in this figure legend, the reader is referred to the web version of this article.)

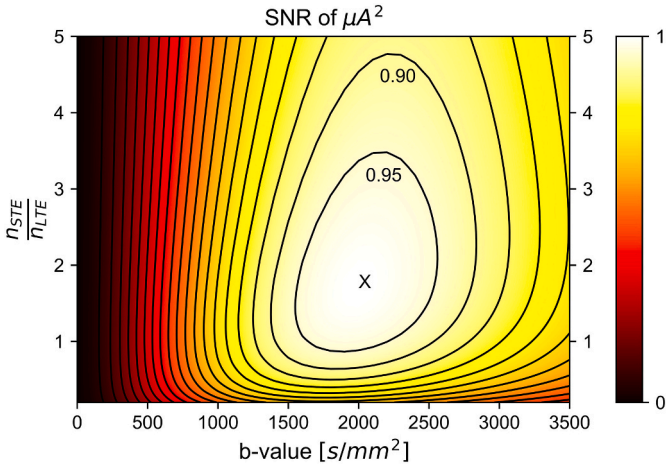

Fig. 3. Simulated μA^2 SNR in white matter as a function of the b-value and the ratio of STE to LTE acquisitions (n_{STE}/n_{LTE}). Though the maximum SNR occurred when b = 2000 s/mm and $n_{STE}/n_{LTE} = 1.7$ (marked by an 'X'), a wide range of parameters yielded SNRs greater than 95% of the maximum SNR, suggesting that there is flexibility in parameter choice when designing a protocol. Notably, a significant drop off in SNR occurred for $n_{STE}/n_{LTE} < 1$, suggesting that image quality is maximized when the number of STE acquisitions is greater than or equal to the number of LTE acquisitions.

4.2. Comparison between different μFA techniques

Example μFA_{gamma} and μFA_{joint} maps computed from the standard subset, as well as μFA_{simp} maps computed from the DTI subset, are depicted in Fig. 5. A sample slice from the raw data, acquired at b = 2000 s/mm^2, is depicted in Supplementary Fig. S1. μFA was observed to be qualitatively consistent across the different techniques and data subsets and image quality was comparable between them. Notably, μFA and μA were observed to be negligible in regions containing only CSF, such as in the lateral ventricles, where diffusion is expected to be isotropic.

Scatter plots and Bland-Altman plots comparing WM μFA using the three different estimation approaches in all volunteers are presented in Fig. 6. Strong linear correlations were observed in the scatter plots comparing each volume, with respective Pearson correlation coefficients of 0.97 (μFA_{gamma} vs. μFA_{joint}), 0.90 (μFA_{gamma} vs. μFA_{simp}), and 0.90 (μFA_{joint} vs. μFA_{simp}). Relative to μFA_{gamma}, the mean WM biases in the other volumes were − 0.11 (μFA_{joint}) and − 0.02 (μFA_{simp}).

4.3. Analysis of repeatability

Bland-Altman plots comparing the test and retest μFA volumes across all volunteers revealed no biases in repeat measurements (Fig. 7). The Pearson correlation coefficients between the test and retest μFA maps were 0.83 (μFA_{gamma}), 0.79 (μFA_{joint}), and 0.84 (μFA_{simp}).

4.4. Minimalistic sequence

Sample μFA, μA^2, and LTE and STE variance maps generated using the minimalistic data subsets are depicted in Fig. 8. Bland-Altman plots comparing the test and retest volumes (not depicted) revealed no biases between the measurements, a CoV of 5%, and a Pearson correlation coefficient of 0.77, demonstrating strong evidence of repeat measurement reliability.

5. Discussion

Microscopic anisotropy mapping has been gaining popularity in neuroimaging studies because it provides a marker of tissue microstructure independent of orientation dispersion. The aims of this work were

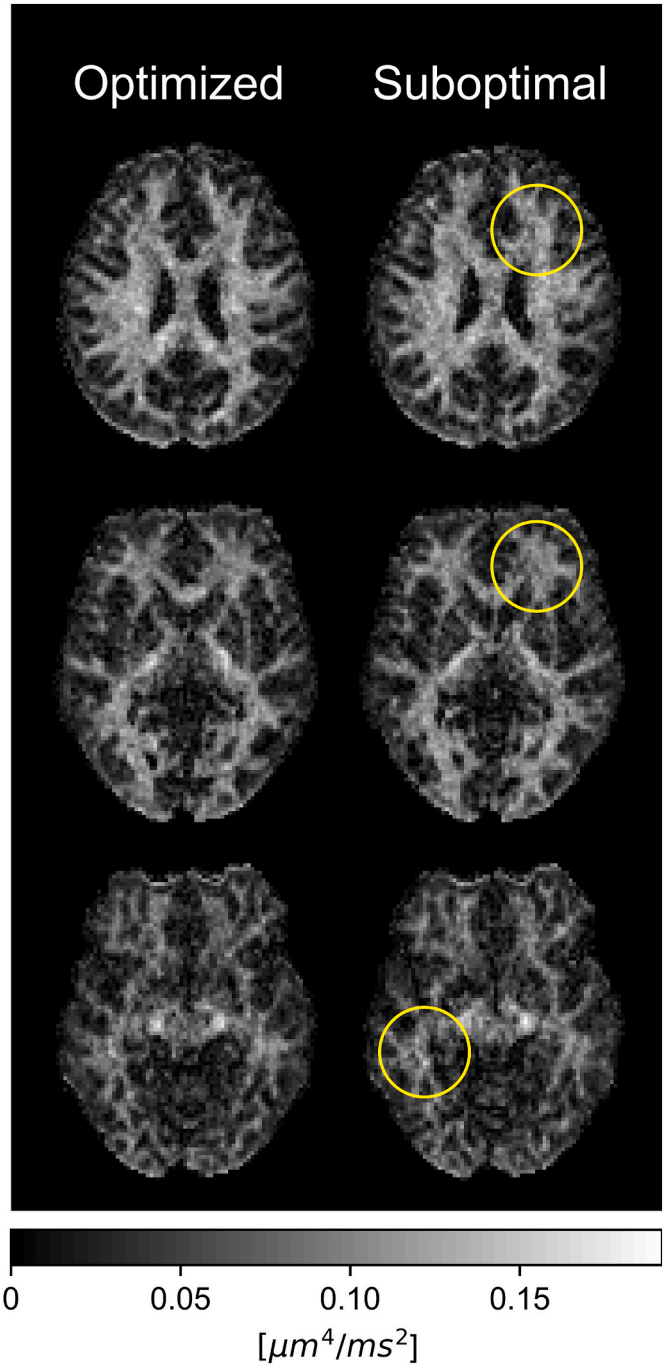

Fig. 4. Example μA^2 images acquired with the standard (left) and suboptimal (right) subsets of the data without denoising. Lower image quality is observed in the right case, with some irregular features highlighted by the yellow circles. Images were acquired with rate 2 in-plane parallel imaging combined with rate 2 simultaneous multislice. (For interpretation of the references to colour in this figure legend, the reader is referred to the web version of this article.)

two-fold: (1) to determine the optimal dMRI parameters (b-value and n_{STE}/n_{LTE}) needed to maximize image quality for a given scan time or number of acquisitions and use this information to design a rapid protocol with <5 min scan time, and (2) to compare the linear regression-based μFA techniques described in this work against the gamma model. The first aim was achieved by directly estimating μA^2 from the cumulant expansion of powder-averaged LTE and STE acquisitions and then estimating the SNR of μA^2 using standard error propagation theory. The optimal b-value of 2000 s/mm^2 falls within the optimal range for DDE

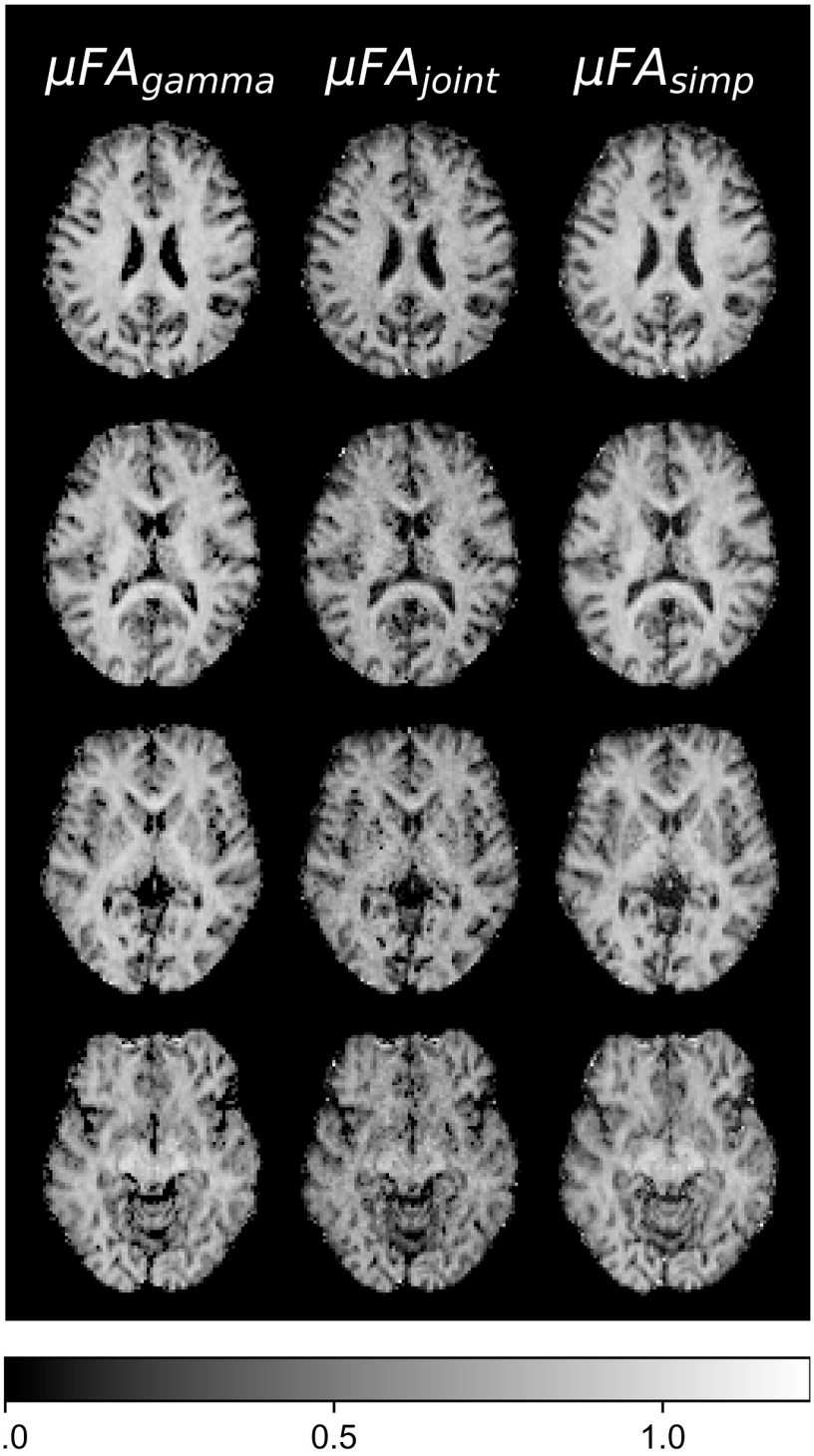

Fig. 5. Example μFA images from one volunteer. Images were acquired using the gamma model with the standard subset (left), joint linear regression with the standard subset (center), and simplified linear regression (i.e., D computed from DTI using only b-values of 100 and 1000 s/mm^2) (right). Comparable image quality is observed for the three methods. Images were acquired with rate 2 in-plane parallel imaging combined with rate 2 simultaneous multislice.

methods; Ianus et al. found that b-values between 2000 and 3000 s/mm^2 are optimal for single-shell DDE estimations of μA because lower b-values result in noisy images while higher b-values result in large biases [36]. The optimal n_{STE}/n_{LTE} (S_{LTE}/S_{STE}) is somewhat intuitive as STE images typically have lower signal than LTE images due to the more rapid signal decrease with b-value. Notably, a steep drop-off in SNR with n_{STE}/n_{LTE} ratios below 1 was observed. These optimization findings were validated by the test-retest CoV ratio between the standard and suboptimal data sets agreeing with the SNR ratio predicted by eq. (10). Notably, these findings are complementary to recommendations for the minimal number of LTE directions to avoid rotational variance [59] and for optimized STE waveforms to minimize the TE [60]. The second aim was achieved by acquiring all the data necessary for all the different μFA volumes in a single acquisition, mapping μFA from different subsets of data, and performing voxelwise comparisons on the maps. Notably, the linear regression approaches described in section 2.2 yielded comparable reliability and strong correspondence with the gamma method when a maximum b-value of 2000 s/mm^2 was used.

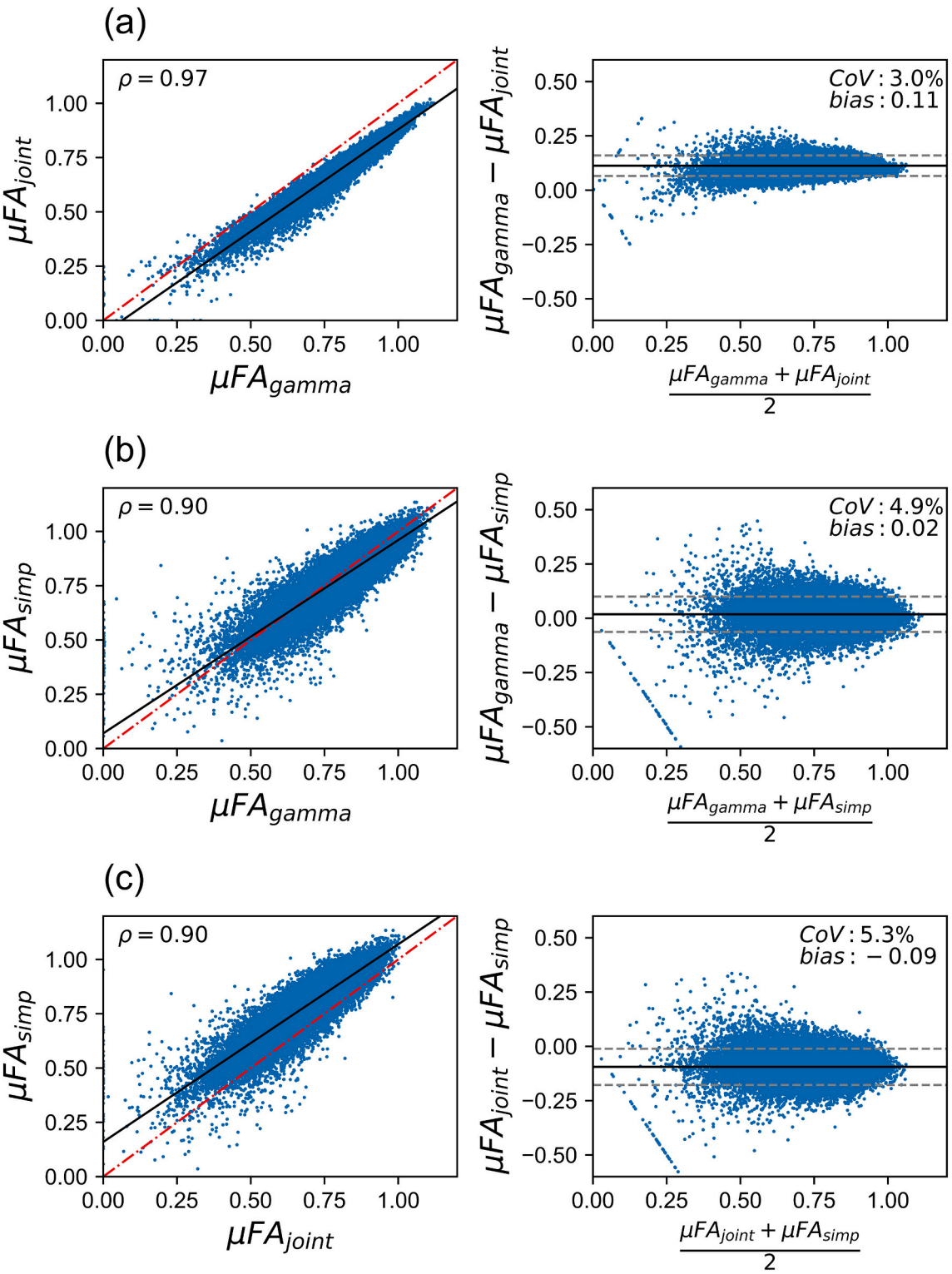

Fig. 6. Voxelwise correlations between μFA estimates acquired using different techniques in white matter (left) and Bland-Altman plots depicting biases between the methods in white matter (right): (a) μFA_{gamma} vs. μFA_{joint}, (b) μFA_{gamma} vs. μFA_{simp}, and (c) μFA_{joint} vs. μFA_{simp}. The dashed red line and solid black line in each of the scatter plots represent the identity and regression lines, respectively. The solid black line in the Bland-Altman plots represents the mean bias, and the dashed grey lines represent the ±1.96 standard deviation lines.

The μFA imaging techniques proposed in this work are suitable for use in clinical research due to the relatively minimalistic acquisition protocols needed to estimate μA^2 and μFA. Furthermore, μFA computation time in the standard subset only took approximately 2 min per volume using joint regression and was virtually instantaneous for simplified regression. When designing a rapid protocol to acquire μFA images using linear regression, the authors recommend using the following steps: (1) acquire enough LTE acquisitions at the highest b-value (e.g. 2000 s/mm^2) to ensure rotational invariance in the powder-averaged signal [59], (2) acquire as many STE acquisitions as possible

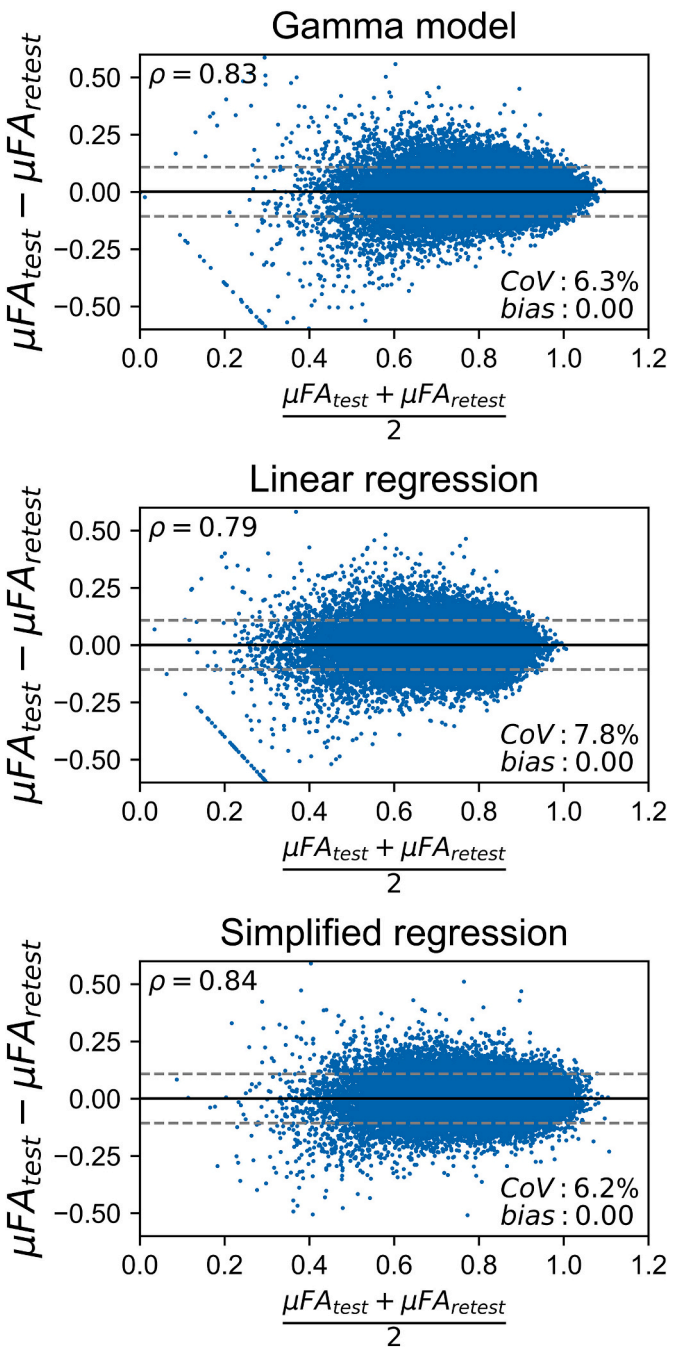

Fig. 7. Bland-Altman plots assessing the test-retest reliability of μFA estimates acquired using different techniques in white matter. The solid black line represents the mean bias, and the dashed grey lines represent the ±1.96 standard deviation lines.

within the scan time limitation to bring the ratio of n_{STE}/n_{LTE} as close to the optimal value (1.7 in this work) as possible, without going below $n_{STE}/n_{LTE} = 1$ to avoid sharply decreasing SNR (Fig. 3), and (3) acquire STE acquisitions at 2–3 lower b-shells for curve fitting. The minimalistic sequence serves as an example of how this procedure can be used to develop a rapid imaging protocol. In designing this protocol, we first, decided to include 16 LTE acquisitions at b = 2000 s/mm^2 to ensure rotational invariance. Next, we opted for 18 STE acquisitions at b = 2000 s/mm^2 to achieve an n_{STE}/n_{LTE} ratio of 1.125. Finally, we included 3 and 6 STE acquisitions at b = 100 and 1000 s/mm^2, respectively, for curve fitting, which resulted in a total acquisition time under 3.3 min. Note that post-processing was performed on this subset after separating it from the rest of the data. Notably, if the number of slices, resolution, and use of parallel imaging for this protocol was set to be the same as the rapid protocol proposed by Nilsson that required 3 min [47], the scan time would have been 2.3 min. Additionally, the joint regression approach requires fewer low b-value acquisitions, which allows for more LTE directions at the highest b-value and potentially results in less error from rotational variance [59]. Nevertheless, this protocol demonstrates that the LTE variance (and thus the linear kurtosis) can be estimated from a set of data containing only one LTE shell and three STE shells when D is assumed to be the same between LTE and STE acquisitions.

In this study, biases were observed in the regression μFA WM maps relative to the measurements produced by the gamma model. The μFA_{joint} metric had a mean bias of −0.11 compared to μFA_{gamma}, while the μFA_{simp} metric was biased against μFA_{gamma} by a modest −0.02. We suspect that the most likely causes of this discrepancy between the techniques are the differences between the models used to fit the data: the implementation of the gamma model used in this work utilizes a soft Heaviside function to constrain the fit to more heavily use the lower b-values, similar to the DTI fit for D in μFA_{simp}. Accordingly, strong correspondence was observed between μFA_{gamma} and μFA_{simp}. Using a full kurtosis fit to estimate D resulted in lower μFA values in the μFA_{joint} volume, which reveals a potential bias in the other two methods that results in physically implausible μFA values that are greater than 1 (see Fig. 7). That said, μFA computed from the eq. (2) approach could also be biased to lower values because the cumulant expansions of the powder-averaged signals were limited to the second order (eqs. (4, 5)), ignoring the effects of higher order terms. Using the mean WM signal data across all volunteers from the sequence optimization dataset (Table 1, Fig. 2) revealed that the second order kurtosis model fit using b-values up to 2000 s/mm^2 underestimated μFA by up to 9.3% compared to a third order fit using b-values up to 3500 s/mm^2. A previous study that used DDE to estimate μA at a single b-value in six different microstructural models [36] reported an underestimation of the metric when acquired at a single b-shell; to remove this bias, the use of a multiple b-shell approach utilizing a higher order cumulant expansion of the dMRI signal can be considered.

Qualitatively, the biases between the different volumes did not have a significant impact on the images as contrast between structures or regions and image quality appeared similar in all the maps. Additionally, voxel-wise comparisons between the maps showed strong linear relationships in WM regions, evidence that the biases between the different techniques are likely scalar or constant. We propose that each of the techniques described in this work may be suitable for use in clinical research under the caveat that studies assessing multiple patients or assessing patients longitudinally should use the same protocol and technique to avoid biases.

There are several limitations potentially affecting the accuracy of this study. The STE sequence used in this work utilizes different gradient waveforms in each diffusion-encoding direction, probing each at slightly different diffusion times and over different trajectories in q-space and potentially giving rise to orientational biases [18]. Given the small microstructural length scales in WM (<10 μm), the long diffusion time regime is likely an appropriate assumption for all 3 waveforms, though future studies may still wish to powder average STE data acquired using different gradient directions. This potential bias is not expected to have impacted our optimization findings or comparisons between regression and the gamma model because they all used identical waveforms. Also, a slightly reduced minimum TE could likely have been achieved with optimized STE waveforms [60], but we implemented a simpler version that can be easily computed online on the scanner. While this may have a slight impact on the optimal b-value, the optimal ratio of STE to LTE acquisitions had no dependence on TE.

A relatively low number of LTE directions were acquired at b = 2000 s/mm^2 in the standard data subsets, which may have slightly reduced the accuracy of the measurements by introducing a directional dependence to the powder-averaged signal [47]. This would not have affected

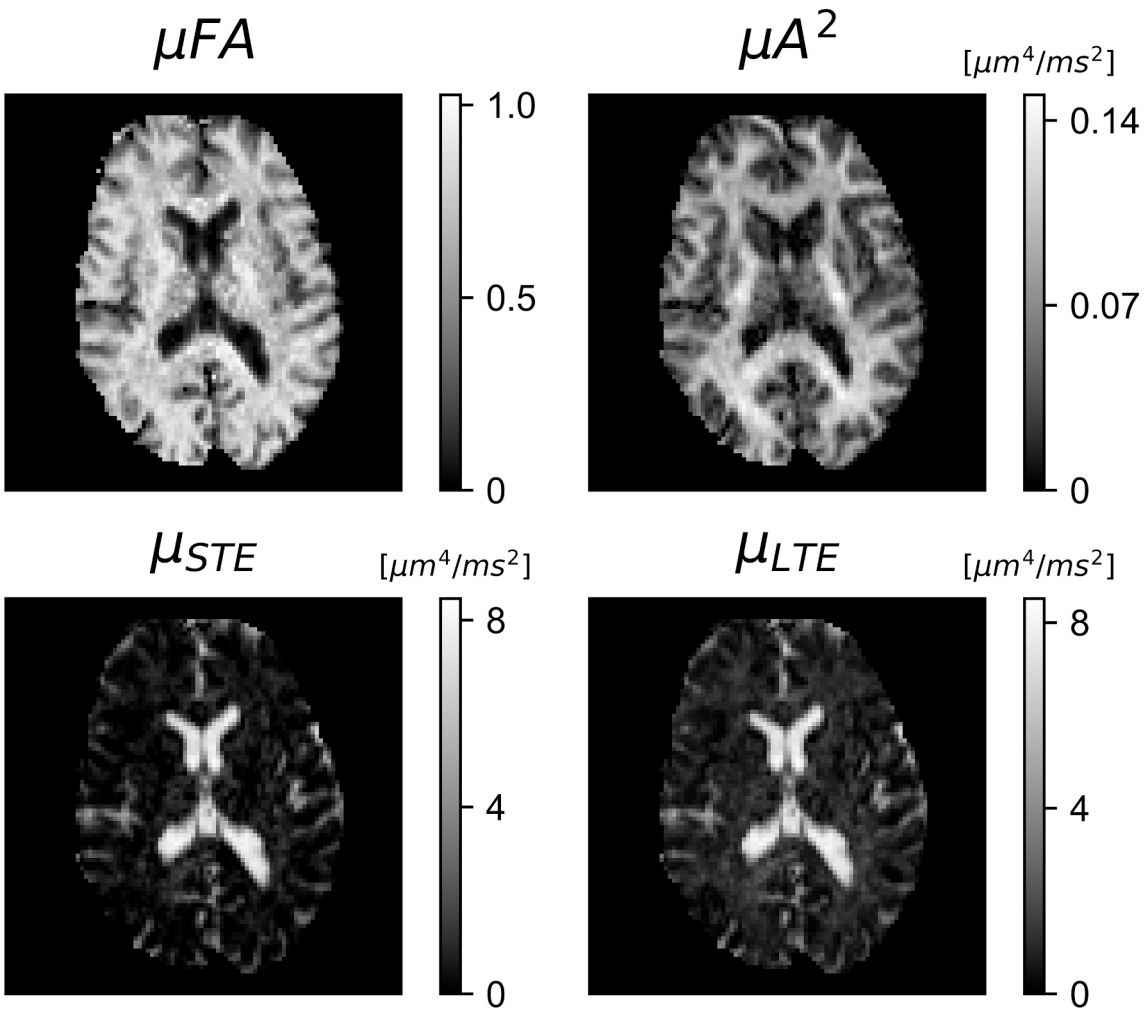

Fig. 8. Example μFA, μA^2, and LTE and STE variance maps acquired using eq. 2 in a subsampled data set: The acquisition comprised of 16 LTE directions at b = 2000 s/mm^2 and 3, 6, and 18 STE directions at b = 100, 1000, and 2000 s/mm^2, respectively. This direction scheme corresponds to a total scan time of approximately 3.3 min with 220 mm × 220 mm × 96 mm coverage at an isotropic 2 mm resolution. All images were normalized to a maximum pixel value of 1. Images were acquired with rate 2 in-plane parallel imaging combined with rate 2 simultaneous multislice.

comparisons between μFA_{joint} and μFA_{gamma}, but the μFA_{simp} volume was computed with more acquisitions at b = 2000 s/mm^2, which may have slightly advantaged measurements of reliability from that volume against the others.

1. The regression technique described herein makes the assumption that the dMRI signal arises only from multiple Gaussian components, which is violated when time-dependent diffusion is not negligible or when microscopic kurtosis is non-vanishing [18]. This potential confound may warrant the use of advanced techniques such as CTI, even at the expense of a longer TE, to yield μFA estimations without these assumptions [19].

6. Conclusion

In conclusion, we have demonstrated an optimized linear regression technique based on the diffusion kurtosis model that enabled full-brain mapping of μFA in a clinically relevant 3.3 min scan time at 3 T. Two implementations of the proposed direct approach were validated against the gamma model, and an approach to determine the optimal maximum b-value and ratio of STE to LTE acquisitions was proposed and validated. Compared to other μFA techniques involving the use of nonconventional pulse sequences, the direct method described herein requires fewer b-shells (and, thus, fewer total directions). Though additional work is necessary to establish the roles of μA and μFA imaging in clinical research settings, the ability to rapidly probe these measurements in vivo opens the door for exploration into their abilities to assess neurodegeneration and other pathologies.

Declaration of Competing Interest

The authors have no interests to declare.

Acknowledgements

This work was supported by Canada Research Chairs [number 950-231993], Canada First Research Excellence Fund to BrainsCAN, the Natural Sciences and Engineering Council of Canada [grant number RGPIN-2018-05448], and Ontario Graduate Scholarships. The authors would also like to thank Ms. Naila Rahman (Western University) for aiding with image registration.

Appendix A. Signal to noise ratio of μA^2 estimation

The variance of μA^2 ($\sigma^2_{\mu A^2}$), assuming equal noise in STE and LTE images and that there is no covariance between the two acquisition types, can be approximated using the error propagation equation. Propagating error from eq. (8) yields:

$$\begin{aligned}\sigma^2_{\mu A^2} &= \left(\frac{\partial \mu A^2}{\partial S_{LTE}}\right)^2 \frac{\sigma^2}{n_{LTE}} + \left(\frac{\partial \mu A^2}{\partial S_{STE}}\right)^2 \frac{\sigma^2}{n_{STE}} \\ &= \frac{\sigma^2}{b^4}\left(\frac{n_{STE}S^2_{STE} + n_{LTE}S^2_{LTE}}{n_{STE}n_{LTE}S^2_{STE}S^2_{LTE}}\right)\end{aligned} \tag{A.1}$$

where σ is the noise in an STE or LTE diffusion-weighted MR image, b is the b-value, n_{LTE} is the number of LTE directions acquired, n_{STE} is the number of STE averages acquired, and S_{LTE} and S_{STE} are the mean signals in LTE and STE acquisitions, respectively. The SNR of a μA^2 image or volume ($SNR_{\mu A^2}$) can be estimated as the μA^2 metric divided by its standard deviation:

$$SNR_{\mu A^2} = \frac{\mu A^2}{\sigma_{\mu A^2}} \tag{A.2}$$

Substituting eqs. (8) and (A.1) into (A.2) yields eq. (10):

$$\begin{aligned}\frac{\mu A^2}{\sigma_{\mu A^2}} &= \frac{\dfrac{ln\left(\dfrac{S_{LTE}}{S_{STE}}\right)}{b^2}}{\sqrt{\dfrac{\sigma^2}{b^4}\left(\dfrac{n_{STE}S^2_{STE} + n_{LTE}S^2_{LTE}}{n_{STE}n_{LTE}S^2_{STE}S^2_{LTE}}\right)}} \\ &= \frac{ln\left(\dfrac{S_{lin}}{S_{iso}}\right)\sqrt{n_{LTE}n_{STE}}S_{LTE}S_{STE}}{\sigma\sqrt{n_{LTE}S^2_{LTE} + n_{STE}S^2_{Ste}}}\end{aligned}$$

To determine the optimal ratio of n_{LTE}/n_{STE} as a function of the mean LTE and STE signal at a single b-value, we can express eq. (A3) in terms of only n_{LTE} and n_{STE}, replacing most other terms with the constant C. We can also confine the total number of acquisitions to an integer value, N, and replace n_{STE} with N-n_{LTE} to reduce the number of unknown variables in the formula. The resulting expression is:

$$\frac{\mu A^2}{\sigma_{\mu A^2}} = \frac{C\sqrt{n_{LTE}(N - n_{LTE})}}{\sqrt{n_{LTE}S^2_{LTE} + (N - n_{LTE})S^2_{STE}}} \tag{A.3}$$

The maxima and minima of eq. (A.3) can be calculated by solving for the roots of the derivative of the SNR equation:

$$\frac{d\left(\frac{\mu A^2}{\sigma_{\mu A^2}}\right)}{dn_{lin}} = C\left(\frac{N - 2n_{LTE}}{2\sqrt{n_{LTE}(N - n_{LTE})}\sqrt{S^2_{STE}(N - n_{LTE}) + S^2_{LTE}n_{LTE}}} - \frac{\sqrt{n_{LTE}(N - n_{LTE})}\left(S^2_{LTE} - S^2_{STE}\right)}{2\left(S^2_{STE}(N - n_{LTE}) + S^2_{LTE}n_{LTE}\right)^{\frac{3}{2}}}\right) \tag{A.4}$$

The roots of (A.4) are $n_{LTE} = NS_{STE}/(S_{STE} - S_{LTE})$ and $n_{LTE} = NS_{STE}/(S_{STE} + S_{LTE})$, the prior of which is not realizable because n_{LTE} would be negative if $S_{STE} < S_{LTE}$. Rearranging the latter yields the optimal ratio of STE to LTE acquisitions:

$$n_{lin} = \frac{NS_{STE}}{S_{STE} + S_{LTE}} = \frac{(n_{LTE} + n_{STE})S_{STE}}{S_{STE} + S_{LTE}}$$

$$\frac{n_{STE}}{n_{LTE}} = \frac{S_{LTE}}{S_{STE}}$$

Appendix B. Supplementary data

Supplementary data to this article can be found online at https://doi.org/10.1016/j.mri.2021.04.015.

References

[1] Stejskal EO, Tanner JE. Spin diffusion measurements: spin echoes in the presence of a time-dependent field gradient. J Chem Phys 1965;42:288–92.
[2] Tanner JE. Pulsed field gradients for NMR spin-Echo diffusion measurements. Rev Sci Instrum 1965;36:1086–7.
[3] Inglese M, Bester M. Diffusion imaging in multiple sclerosis: research and clinical implications. NMR Biomed 2010;23:865–72. https://doi.org/10.1002/nbm.1515.
[4] Rovaris M, Gass A, Bammer R, Hickman SJ, Ciccarelli O, Miller DH, et al. Diffusion MRI in multiple sclerosis. Neurology 2005;65:1526–32.
[5] Zhang Y, Schuff N, Du A-T, Rosen HJ, Kramer JH, Gorno-Tempini ML, et al. White matter damage in frontotemporal dementia and Alzheimer's disease measured by diffusion MRI. Brain 2009;132:2579–92.
[6] van Everdingen KJ, van der Grond J, Kappelle LJ, Ramos LM, Mali WP. Diffusion-weighted magnetic resonance imaging in acute stroke. Stroke 1998;29:1783–90.
[7] Basser PJ, Mattiello J, LeBihan D. MR diffusion tensor spectroscopy and imaging. Biophys J 1994;66:259–67.
[8] Basser PJ. Inferring microstructural features and the physiological state of tissues from diffusion-weighted images. NMR Biomed 1995;8:333–44.
[9] Frisken BJ. Revisiting the method of cumulants for the analysis of dynamic light-scattering data. Appl Opt 2001;40:4087–91.

[10] Johansen-Berg H, Behrens TEJ. Diffusion MRI: From Quantitative Measurement to In Vivo Neuroanatomy. 2nd ed. Academic Press; 2013.
[11] Shemesh N, Adiri T, Cohen Y. Probing microscopic architecture of opaque heterogeneous systems using double-pulsed-field-gradient NMR. J Am Chem Soc 2011;133:6028–35.
[12] Lundell H, Nilsson M, Dyrby TB, Parker GJM, Cristinacce PLH, Zhou F-L, et al. Multidimensional diffusion MRI with spectrally modulated gradients reveals unprecedented microstructural detail. Sci Rep 2019;9:9026.
[13] de Swiet TM, Mitra PP. Possible systematic errors in single-shot measurements of the trace of the diffusion tensor. J Magn Reson B 1996;111:15–22.
[14] Jensen JH, Helpern JA, Ramani A, Lu H, Kaczynski K. Diffusional kurtosis imaging: the quantification of non-gaussian water diffusion by means of magnetic resonance imaging. Magn Reson Med Off J Int Soc Magn Reson Med 2005;53:1432–40.
[15] Wang J-J, Lin W-Y, Lu C-S, Weng Y-H, Ng S-H, Wang C-H, et al. Parkinson disease: diagnostic utility of diffusion kurtosis imaging. Radiology 2011;261:210–7.
[16] Falangola MF, Jensen JH, Babb JS, Hu C, Castellanos FX, Di Martino A, et al. Age-related non-Gaussian diffusion patterns in the prefrontal brain. J Magn Reson Imaging 2008;28:1345–50. https://doi.org/10.1002/jmri.21604.
[17] Fieremans E, Benitez A, Jensen JH, Falangola MF, Tabesh A, Deardorff RL, et al. Novel white matter tract integrity metrics sensitive to Alzheimer disease progression. Am J Neuroradiol 2013;34:2105–12. https://doi.org/10.3174/ajnr.a3553.
[18] Jespersen SN, Olesen JL, Ianuş A, Shemesh N. Effects of nongaussian diffusion on "isotropic diffusion" measurements: an ex-vivo microimaging and simulation study. J Magn Reson 2019;300:84–94.
[19] Henriques RN, Jespersen SN, Shemesh N. Correlation tensor magnetic resonance imaging. Neuroimage 2020;211:116605.
[20] Burcaw LM, Fieremans E, Novikov DS. Mesoscopic structure of neuronal tracts from time-dependent diffusion. Neuroimage 2015;114:18–37.
[21] Jones DK, Knösche TR, Turner R. White matter integrity, fiber count, and other fallacies: the do's and don'ts of diffusion MRI. Neuroimage 2013;73:239–54.
[22] Szczepankiewicz F, Lasič S, van Westen D, Sundgren PC, Englund E, Westin CF, et al. Quantification of microscopic diffusion anisotropy disentangles effects of orientation dispersion from microstructure: applications in healthy volunteers and in brain tumors. Neuroimage 2015;104:241–52.
[23] Fieremans E, Jensen JH, Helpern JA. White matter characterization with diffusional kurtosis imaging. Neuroimage 2011;58:177–88.
[24] Jespersen SN, Lundell H, Sønderby CK, Dyrby TB. Orientationally invariant metrics of apparent compartment eccentricity from double pulsed field gradient diffusion experiments. NMR Biomed 2013;26:1647–62.
[25] Lasič S, Szczepankiewicz F, Eriksson S, Nilsson M, Topgaard D. Microanisotropy imaging: quantification of microscopic diffusion anisotropy and orientational order parameter by diffusion MRI with magic-angle spinning of the q-vector. Front Phys 2014;2. https://doi.org/10.3389/fphy.2014.00011.
[26] Shemesh N, Jespersen SN, Alexander DC, Cohen Y, Drobnjak I, Dyrby TB, et al. Conventions and nomenclature for double diffusion encoding NMR and MRI. Magn Reson Med 2016;75:82–7.
[27] Novikov DS, Fieremans E, Jespersen SN, Kiselev VG. Quantifying brain microstructure with diffusion MRI: theory and parameter estimation. NMR Biomed 2019;32:e3998.
[28] Kaden E, Kruggel F, Alexander DC. Quantitative mapping of the per-axon diffusion coefficients in brain white matter. Magn Reson Med 2016;75:1752–63.
[29] Kaden E, Kelm ND, Carson RP, Does MD, Alexander DC. Multi-compartment microscopic diffusion imaging. Neuroimage 2016;139:346–59.
[30] Cory DG, Garroway AN, Miller JB. Applications of spin transport as a probe of local geometry. In: Abstracts of Papers of the American Chemical Society. Vol. 199. 1155 16TH ST, NW, Washington, DC 20036: Amer Chemical Soc; 1990. p. 105-POLY.
[31] Eriksson S, Lasič S, Nilsson M, Westin C-F, Topgaard D. NMR diffusion-encoding with axial symmetry and variable anisotropy: distinguishing between prolate and oblate microscopic diffusion tensors with unknown orientation distribution. J Chem Phys 2015;142:104201. https://doi.org/10.1063/1.4913502.
[32] Westin C-F, Knutsson H, Pasternak O, Szczepankiewicz F, Özarslan E, van Westen D, et al. Q-space trajectory imaging for multidimensional diffusion MRI of the human brain. Neuroimage 2016;135:345–62.
[33] Lampinen B, Szczepankiewicz F, Mårtensson J, van Westen D, Sundgren PC, Nilsson M. Neurite density imaging versus imaging of microscopic anisotropy in diffusion MRI: a model comparison using spherical tensor encoding. Neuroimage 2017;147:517–31.
[34] Henriques RN, Jespersen SN, Shemesh N. Microscopic anisotropy misestimation in spherical-mean single diffusion encoding MRI. Magn Reson Med 2019. https://doi.org/10.1002/mrm.27606.
[35] Mitra PP. Multiple wave-vector extensions of the NMR pulsed-field-gradient spin-echo diffusion measurement. Phys Rev B Condens Matter 1995;51:15074–8.
[36] Ianuş A, Jespersen SN, Serradas Duarte T, Alexander DC, Drobnjak I, Shemesh N. Accurate estimation of microscopic diffusion anisotropy and its time dependence in the mouse brain. Neuroimage 2018;183:934–49.
[37] Ozarslan E, Basser PJ. Microscopic anisotropy revealed by NMR double pulsed field gradient experiments with arbitrary timing parameters. J Chem Phys 2008;128:154511.
[38] Lawrenz M, Finsterbusch J. Mapping measures of microscopic diffusion anisotropy in human brain white matter in vivo with double-wave-vector diffusion-weighted imaging. Magn Reson Med 2015;73:773–83.
[39] Yang G, Tian Q, Leuze C, Wintermark M, McNab JA. Double diffusion encoding MRI for the clinic. Magn Reson Med 2018;80:507–20.
[40] Kerkelä L, Henriques RN, Hall MG, Clark CA, Shemesh N. Validation and noise robustness assessment of microscopic anisotropy estimation with clinically feasible double diffusion encoding MRI. Magn Reson Med 2020;83:1698–710.
[41] Baron CA, Lebel RM, Wilman AH, Beaulieu C. The effect of concomitant gradient fields on diffusion tensor imaging. Magn Reson Med 2012;68:1190–201.
[42] Szczepankiewicz F, Westin C, Nilsson M. Maxwell-compensated design of asymmetric gradient waveforms for tensor-valued diffusion encoding. Magn Reson Med 2019;82:mrm.27828.
[43] Eriksson S, Lasic S, Topgaard D. Isotropic diffusion weighting in PGSE NMR by magic-angle spinning of the q-vector. J Magn Reson 2013;226:13–8.
[44] Szczepankiewicz F, van Westen D, Englund E, Westin C-F, Ståhlberg F, Lätt J, et al. The link between diffusion MRI and tumor heterogeneity: mapping cell eccentricity and density by diffusional variance decomposition (DIVIDE). Neuroimage 2016;142:522–32.
[45] Westin C-F, Szczepankiewicz F, Pasternak O, Ozarslan E, Topgaard D, Knutsson H, et al. Measurement tensors in diffusion MRI: generalizing the concept of diffusion encoding. Med Image Comput Comput Assist Interv 2014;17:209–16.
[46] Nery F, Szczepankiewicz F, Kerkelä L, Hall MG, Kaden E, Gordon I, et al. In vivo demonstration of microscopic anisotropy in the human kidney using multidimensional diffusion MRI. Magn Reson Med 2019;82:2160–8.
[47] Nilsson M, Szczepankiewicz F, Brabec J, Taylor M, Westin C, Golby A, et al. Tensor-valued diffusion MRI in under 3 minutes: an initial survey of microscopic anisotropy and tissue heterogeneity in intracranial tumors. Magn Reson Med 2019. https://doi.org/10.1002/mrm.27959.
[48] Shemesh N. Axon diameters and myelin content modulate microscopic fractional anisotropy at short diffusion times in fixed rat spinal cord. Front Phys 2018;6. https://doi.org/10.3389/fphy.2018.00049.
[49] Xing D, Papadakis NG, Huang CLH, Lee VM, Carpenter TA, Hall LD. Optimised diffusion-weighting for measurement of apparent diffusion coefficient (ADC) in human brain. Magn Reson Imaging 1997;15:771–84.
[50] Bevington PR, Robinson DK, Blair JM, Mallinckrodt AJ, McKay S. Data reduction and error analysis for the physical sciences. Comput Phys 1993;7:415–6.
[51] Andersson JLR, Sotiropoulos SN. An integrated approach to correction for off-resonance effects and subject movement in diffusion MR imaging. Neuroimage 2016;125:1063–78.
[52] Wansapura JP, Holland SK, Dunn RS, Ball WS. NMR relaxation times in the human brain at 3.0 tesla. J Magn Reson Imaging 1999;9:531–8.
[53] Baron C, Arezza NJJ. Test-retest data repository for spherical tensor encoding. https://osf.io/etkgx/; 2020.
[54] Veraart J, Novikov DS, Christiaens D, Ades-Aron B, Sijbers J, Fieremans E. Denoising of diffusion MRI using random matrix theory. Neuroimage 2016;142:394–406.
[55] Zhang Y, Brady M, Smith S. Segmentation of brain MR images through a hidden Markov random field model and the expectation-maximization algorithm. IEEE Trans Med Imaging 2001;20:45–57.
[56] Chen DQ, Dell'Acqua F, Rokem A, Garyfallidis E. Diffusion weighted image co-registration: investigation of best practices. BioRxiv 2019. https://doi.org/10.1101/864108.
[57] Jones DK, Horsfield MA, Simmons A. Optimal strategies for measuring diffusion in anisotropic systems by magnetic resonance imaging. Magn Reson Med 1999;42:515–25.
[58] Nilsson M, Szczepankiewicz F, Lampinen B, Ahlgren A, de Almeida Martins JP, Lasic S, et al. An open-source framework for analysis of multidimensional diffusion MRI data implemented in MATLAB. In: Proc. Intl. Soc. Mag. Reson. Med.; 2018.
[59] Szczepankiewicz F, Sjölund J, Ståhlberg F, Lätt J, Nilsson M. Tensor-valued diffusion encoding for diffusional variance decomposition (DIVIDE): technical feasibility in clinical MRI systems. PLoS One 2019;14:e0214238.
[60] Szczepankiewicz F, Westin C-F, Nilsson M. Gradient waveform design for tensor-valued encoding in diffusion MRI. J Neurosci Methods 2021;348:109007.